RESEARCH PAPER

Effect of partial and full post-weld heat treatments on microstructure and mechanical properties of IN738LC joint by electron beam welding

Ke Han[1,2] · Houqin Wang[2] · Binggang Zhang[2] · Xiaopeng Li[3] · Jian Zhao[4] · Kun Shi[5] · Hongwen Liu[5]

Abstract

This work explored the microstructure, mechanical properties, and the related fracture mechanism of electron beam welded (EBW) IN738LC joints subjected to partial post-weld heat treatment (P-PWHT) and full post-weld heat treatment (F-PWHT). The two PWHT schedules produced a significant effect on the microstructure and mechanical properties of IN738LC joints. The fusion zone (FZ) presented a similar microstructure with BM, composed of duplex-sized γ′ particles, blocky MC carbides, and continuous M23C6 carbides. While F-PWHT resulted in the complete dissolution of primary γ′ particles and unimodal-spheroidal γ′ particles were obtained in IN738LC joint. The size and amount of γ′ particles in FZ and BM of the joints after F-PWHT were higher than that of IN738LC joints subjected to P-PWHT. In addition, F-PWHT also facilitated the dissolution of MC carbides, releasing more free C atoms. High amount of M23C6 carbides consequentially formed along grain boundaries (GBs) in IN738LC joints. Compared with F-PWHT, the formation of duplex-sized γ′ particles and less M23C6 carbides in FZ and BM weakened the tensile strength (900 °C) but improved the elongation (16.6%) of P-PWHTed joints. The retained primary γ′ particles and minor M23C6 carbides in FZ of IN738LC joints after P-PWHT retarded the GB sliding, bringing about a higher stress-rupture life, about 2.5 h (900 °C/350 MPa).

Keywords IN738LC superalloy · EBW · Post-weld heat treatment · Microstructure · Stress-rupture life

✉ Houqin Wang
   wanghouqin@hit.edu.cn

✉ Binggang Zhang
   zhangbg@hit.edu.cn

1 School of Materials Science & Engineering, Jiangsu University, Zhenjiang 212013, People's Republic of China

2 State Key Laboratory of Advanced Welding and Joining, Harbin Institute of Technology, Harbin 150001, People's Republic of China

3 College of Materials Science and Technology, Nanjing University of Science and Technology, Nanjing 210014, People's Republic of China

4 College of Materials Engineering, Shanghai University of Engineering Science, Shanghai 201620, People's Republic of China

5 Sany Heavy Machine Co., Ltd, Kun Shan 215300, People's Republic of China

1 Introduction

IN738 superalloy achieves exceptional comprehensive properties of high-temperature strength, creep resistance, fatigue performance, oxidation, and corrosion resistance due to the high amount of ordered γ′-Ni$_3$(Al,Ti) precipitates from the addition of Al and Ti elements [1]. Therefore, IN738 superalloy has been widely applied in the hot-section components of land-based gas turbine and aircraft engines [2, 3]. But the hot-section components are likely to premature failure owing to the severe service environment [4]. Fusion welding presents economic, flexible, and highly efficient advantages in repairing the damaged components rather than entire replacement. In view of the extremely high energy density, large depth-to-width ratio, minimizable distortion, and minor contamination, EBW shows an outstanding prospect in joining and repairing various alloys [5].

It has been reported that PWHT mainly produces multiple effects: (1) relief of welding residual stress; (2) homogenization of microstructure and composition; and (3) reprecipitation and growth of secondary phases in FZ and HAZ of nickel-based

joints by fusion welding [6, 7]. Based on the solvus temperature of γ′ phases in nickel-based superalloy, two kinds of heat treatment processes composed of P-PWHT (partial solution and aging heat treatment) and F-PWHT (full solution plus aging heat treatment) were put forward [8, 9]. Balikci et al. discussed the microstructural evolution of IN738LC superalloy after different heat treatments. A duplex-precipitate microstructure was obtained after 1120 °C/2 h solution treatment, while the complete dissolution of γ′ precipitates was observed after 1235 °C/2 h solution treatment [10]. Monti et al. investigated the effect of rejuvenation treatment (super-solution+double aging treatment) on microstructure and mechanical properties of IN738 superalloy [11]. The rejuvenation treatment could restore the microstructure (bimodal γ′ precipitates) of the damaged IN738 superalloy, and the creep duration of IN738 superalloy after rejuvenation treatment was longer than that of the virgin material. Wangyao et al. discussed the effect of PWHT on the microstructure of IN738 joint by TIG. With the increase of solution temperature (1125 °C→1205 °C), the size of γ′ precipitates decreased while the γ′ amount decreased [12]. Jurado et al. found that a large amount of γ′ particles and M23C6 carbides precipitated from FZ of as-weld joint subjected to P-PWHT (1100 °C/2 h+860 °C/16 h), resulting in the highest micro-hardness (425HV) [13]. Wang et al. reported that bimodal-sized γ′ particle and moderate MC carbides in IN738LC EBWed joint subjected to partial solutionizing (1125 °C/2 h) showed excellent mechanical properties than that of IN738LC joint with full solutionizing [14]. According to the above literatures, the current investigations emphasized the microstructural evolution of IN738 joints after PWHT. Few reports expounded the relation between microstructure and mechanical properties of IN738 joints subjected to P-PWHT and F-PWHT. Therefore, we mainly analyzed the precipitation behavior of second phases in IN738LC EBWed joints after P-PWHT (1125 °C/2 h/air cooling (AC)+850 °C/24 h/AC) and F-PWHT (1175 °C/2 h/AC+850 °C/24 h/AC) schedules in this work. Subsequently, the elevated temperature mechanical properties of IN738LC joints subjected to P-PWHT and F-PWHT were tested and we also discussed the fracture mechanism of IN738LC joints.

2 Materials and methods

The commercially low-carbon Inconel 738 (abbreviated as IN738LC superalloy) is used in this work and provided by Beijing Institute of Aerial Materials. The nominal chemical composition of base metal (BM) is

listed as in Table 1. The microstructure of BM is shown in Fig. 1. Various precipitates including bimodal-sized γ′ particles, fan-like γ/γ′ eutectic, and white blocky phase were observed. The statistical data in Fig. 1d and e indicated that the sizes of γ′ particles were around 99 nm and 550 nm, respectively. The smaller γ′ particles presented spherical shape and were distributed in dendrite core region (DCR) and interdendritic region (IDR), which was called as secondary γ′ phase, while the larger γ′ particles mainly distributed in IDR exhibited irregular shape, called as primary γ′ phase. In addition, the results of energy dispersive spectrometer (EDS) in Fig. 1c revealed that the white blocky phase was rich in Ti, Nb, and Ta, consistent with the composition of MC carbide [15].

The raw specimens were fabricated into plates with a dimension of 65 mm × 30 mm × 2 mm. The surfaces of BMs were polished by SiC sandpaper and cleaned with ethanol. EBW was performed with MEDARD45 equipment (France TECHMETA) with the following process parameters: accelerating voltage of 55 kV, beam current of 10 mA, welding speed of 10 mm/s, focus current of 2460 mA (surface focus), and vacuum degree of 5×10^{-2} Pa.

As known from the previous report [16], the γ′ solvus temperature of GTD-111 superalloy was between 1120 and 1175 °C. Wang et al. have also proved that γ′ precipitates in IN738LC joint were dissolved completely when treated at 1175 °C for 2 h [14]. As a result, two kinds of PWHT schedules (P-PWHT and F-PWHT) were adopted, as shown in Table 2. In order to avoid the oxidation of IN738LC joints, vacuum PWHT was applied with evacuated quartz tube. The as-weld specimens were put into the heat treatment furnace when the furnace temperature reached the set temperature during PWHT process, as depicted in Fig. 2.

The specimens subjected to PWHT were cut along the cross-section by electrical discharge machining, and then grinded and polished by SiC sandpapers and polishing agent. Subsequently, the metallographic specimens (8 mm × 2 mm × 2 mm) were electrochemically etched by 12 ml H₃PO₄ + 40 ml HNO₃ + 48 ml H₂SO₄ solution at 5 V for 3 s. The cross-section morphologies of IN738LC joints were examined by optical microscope (OM, VHX-1000E). The shape, size, and content of various precipitates in IN738LC joints were observed by scanning electron microscope (SEM, SUPRA55). Moreover, the phase structure and composition of M23C6 carbides in GBs were characterized by field emission transmission electron microscope

Table 1 Nominal chemical composition (*wt.*%) of IN738LC superalloy

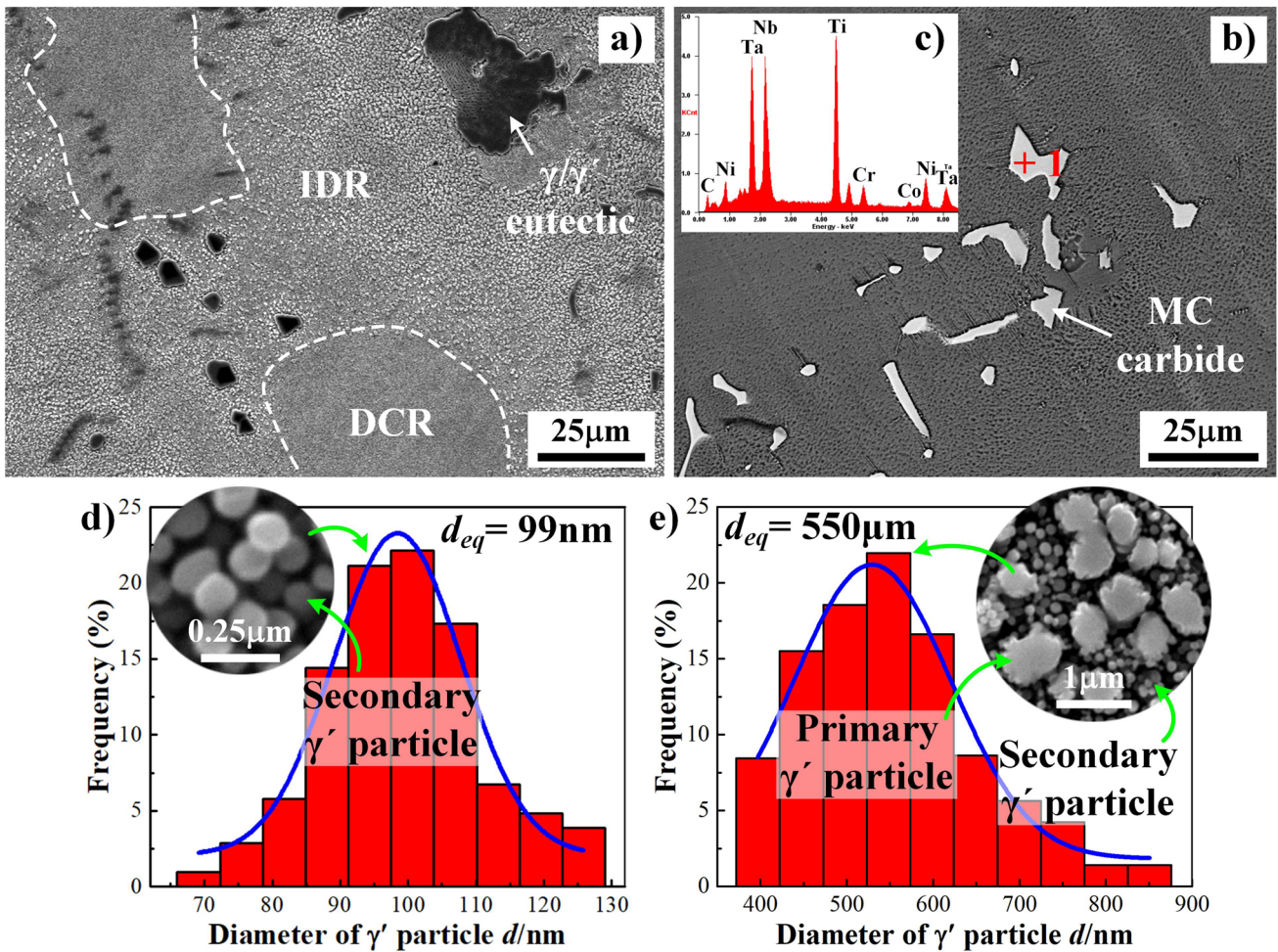| Elements	C	Cr	Co	Nb	W	Zr	Mo	Al	Ti	B	Fe	Ta	Ni
IN738LC	0.11	15.84	8.50	0.92	2.48	0.04	1.88	3.46	3.47	0.012	0.07	1.69	Bal

Fig. 1 IN738LC superalloy microstructure: **a** low-power microstructure; **b** morphology and **c** EDS mapping of MC carbide; equivalent diameter of **d** secondary γ′ particle and **e** primary γ′ particle

Table 2 PWHT process parameters for the IN738LC joints by EBW

	Solution treatment			Aging treatment		
	Temperature T/°C	Holding time t/h	Cooling method	Temperature T/°C	Holding time t/h	Cooling method
P-PWHT	1125	2	Air cooling (AC)	850	24	AC
F-PWHT	1175					

(TEM, FEI Talos F200X). The mechanical properties of IN738LC joints were evaluated by tensile test (900 °C) and stress-rupture test (900 °C/350 MPa). The sample dimensions are shown in Fig. 3. The tensile test and stress-rupture test were conducted by INSTRON-5500R machine and RDL100 machine, respectively. Three samples were tested to ensure the reliability and reproducibility of the test results.

3 Results and discussion

3.1 Microstructural evolution of IN738LC joints

3.1.1 FZ

The microstructural morphologies of BM and FZ in IN738LC joints subjected to different PWHTs are shown
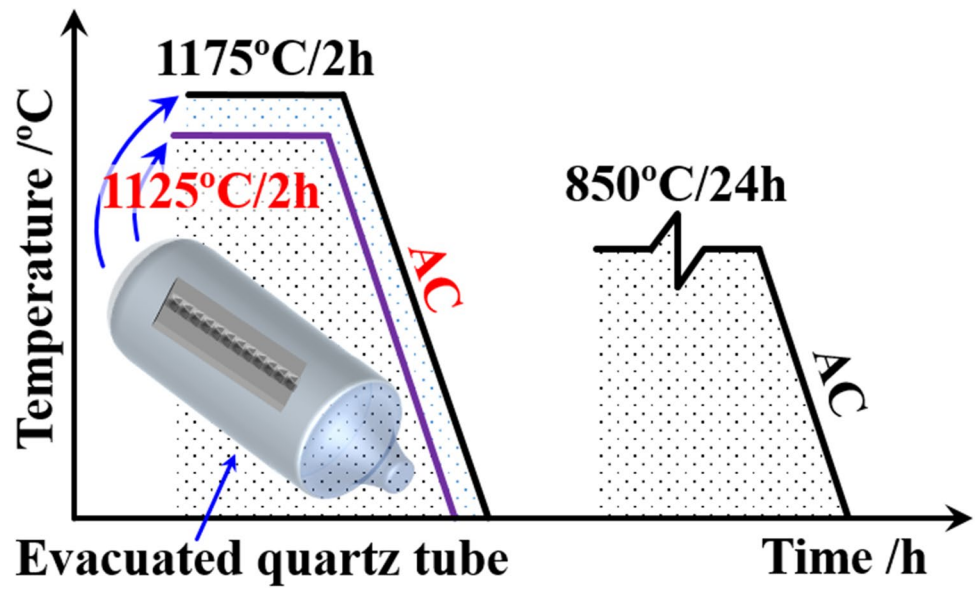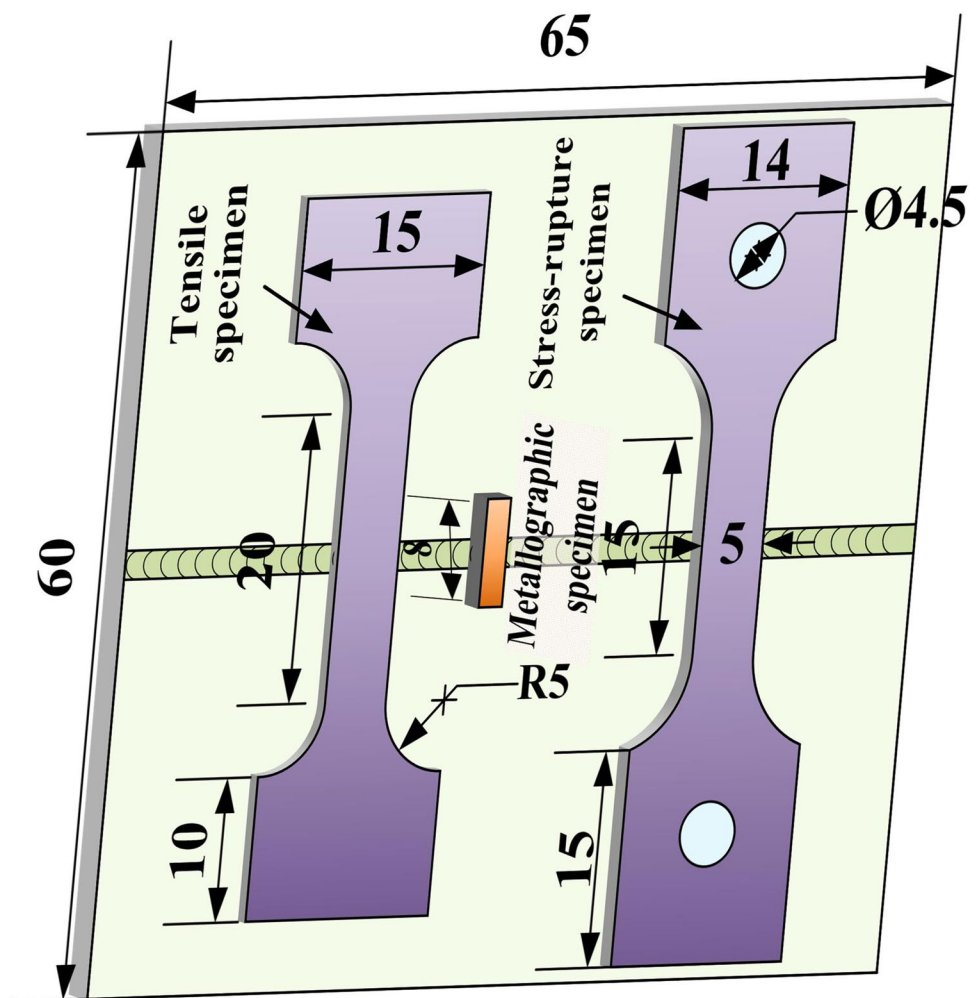
Fig. 2 The flowchart of PWHT
process

Fig. 3 Dimensions of welding
specimens, metallographic spec-
imens, and tensile specimens

in Fig. 4. Compared with the as-weld joint [17], FZ was decorated with a large amount of precipitates including γ′ particles, γ/γ′ eutectic, and carbides. When IN738LC joint was subjected to P-PWHT, dual-sized γ′ particles in FZ were obvious. Similar to the BM microstructure, the primary γ′ particles were mainly accumulated in the IDR and GBs and presented irregular-block shape. But the size of primary γ′ particles in GBs was larger than that in IDR, which was due to the composition segregation of γ′-forming elements (Al, Ti, etc.) [11]. The secondary γ′ particles were distributed in DCR. It is notable that the primary γ′ particles in IDR of FZ were completely dissolved and only trace of primary γ′ particles was visible in GBs of IN738LC joint after F-PWHT, as shown in Fig. 4a2. As known from Fig. 4a2 and d2, the coarse γ′ particles in GBs originated from the growth and ripening of precipitate in the process of aging treatment. Table 3 displays the size and volume fraction of γ′ particles in FZ. It is clear that the size and content of γ′ particles in FZ of IN738LC joint subjected to P-PWHT were higher than that undergoing F-PWHT. He et al. found that the γ′-forming elements were released by the complete dissolution of primary γ′ particles and diffused into matrix during the process of solution treatment [18]. As a result, high density of γ′ precipitates nucleated in FZ. Moreover, the enrichment of γ′-forming elements in matrix also facilitated the growth of γ′ precipitates. Therefore, larger size and higher amount of γ′ particles were distributed in the FZ of IN738LC joint subjected to F-PWHT. Apart from the formed γ′ particles, γ/γ′ eutectic was also produced along GBs, as seen in Fig. 4c 1 and c2. Li et al. [19] and

Table 3 γ′ size and content of BM and FZ in IN738LC joints after different PWHTs

	Equivalent diameter/nm		Volume fraction (%)	
	Primary γ′	Secondary γ′	Primary γ′	Secondary γ′
P-PWHT	360	95.63	6.16	47.83
F-PWHT	/	105.3	/	55.1

Zhang et al. [20] reported that the γ/γ′ eutectic temperature was between 1270 and 1290 °C, which was higher than solution temperature (1125 °C and 1175 °C). Therefore, fine γ/γ′ eutectic precipitated along GBs in as-weld joint grew continuously during PWHT.

In addition, block and continuous precipitates were visible in FZ of IN738LC joints subjected to P-PWHT and F-PWHT, as shown in Fig. 5. TEM was applied to characterize the elemental distribution and phase structure of continuous precipitates. The results are exhibited in Fig. 5b–d. It is obvious that Cr element was enriched in the continuous precipitates (Fig. 5c). Dong et al. pointed out that the Cr-rich precipitates were $M_{23}C_6$ carbides (M was referred to Cr and Mo elements) [21]. The diffraction patterns (Fig. 5d) of Cr-rich precipitates were further determined as FCC $M_{23}C_6$ carbides. Figure 5c also shows that $M_{23}C_6$ carbides obeyed the cube-on-cube orientation relationship with γ-Ni matrix: $\{001\}_{M_{23}C_6 \, M_{23}C_6}//\{001\}_\gamma$ and $<001>_{M_{23}C_6}//<001>_\gamma$. This is due to the same crystal structure (FCC) between $M_{23}C_6$ carbide and γ-Ni matrix and the crystal lattice parameter of $M_{23}C_6$ carbide was three times of γ-Ni. Two classical formation mechanisms of $M_{23}C_6$ carbides consisting of

Fig. 4 FZ microstructure in IN738LC joints subjected to different PWHTs: P-PWHT: **a1** low-magnification microstructure; **b1** secondary γ′ particles; **c1** γ/γ′ eutectic; **d1** 1125 °C/2 h; F-PWHT: **a2** low-magnification microstructure; **b2** secondary γ′ particles; **c2** γ/γ′ eutectic; **d2** 1175 °C/2 h
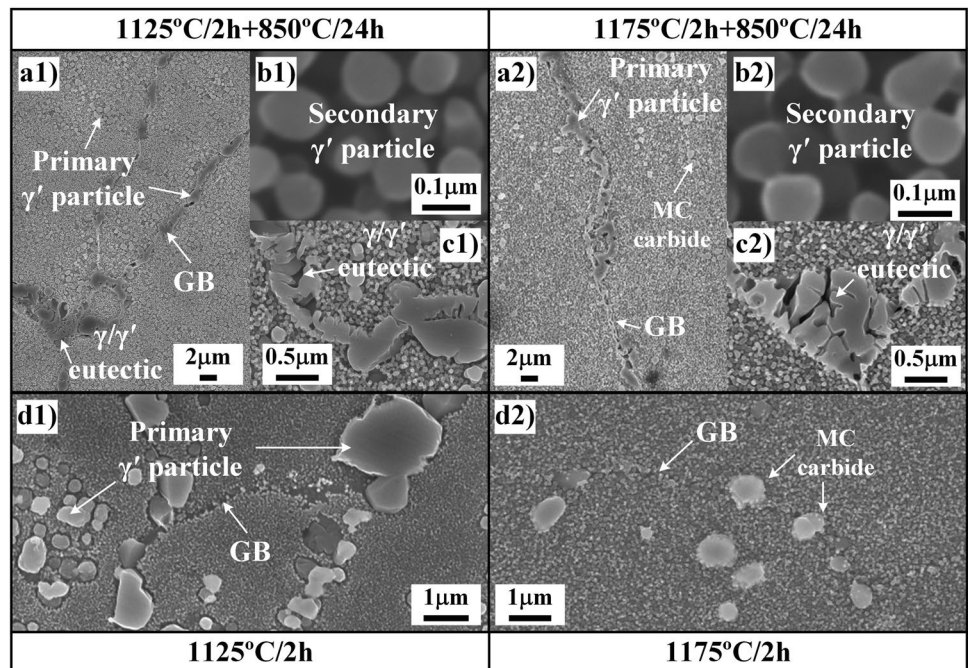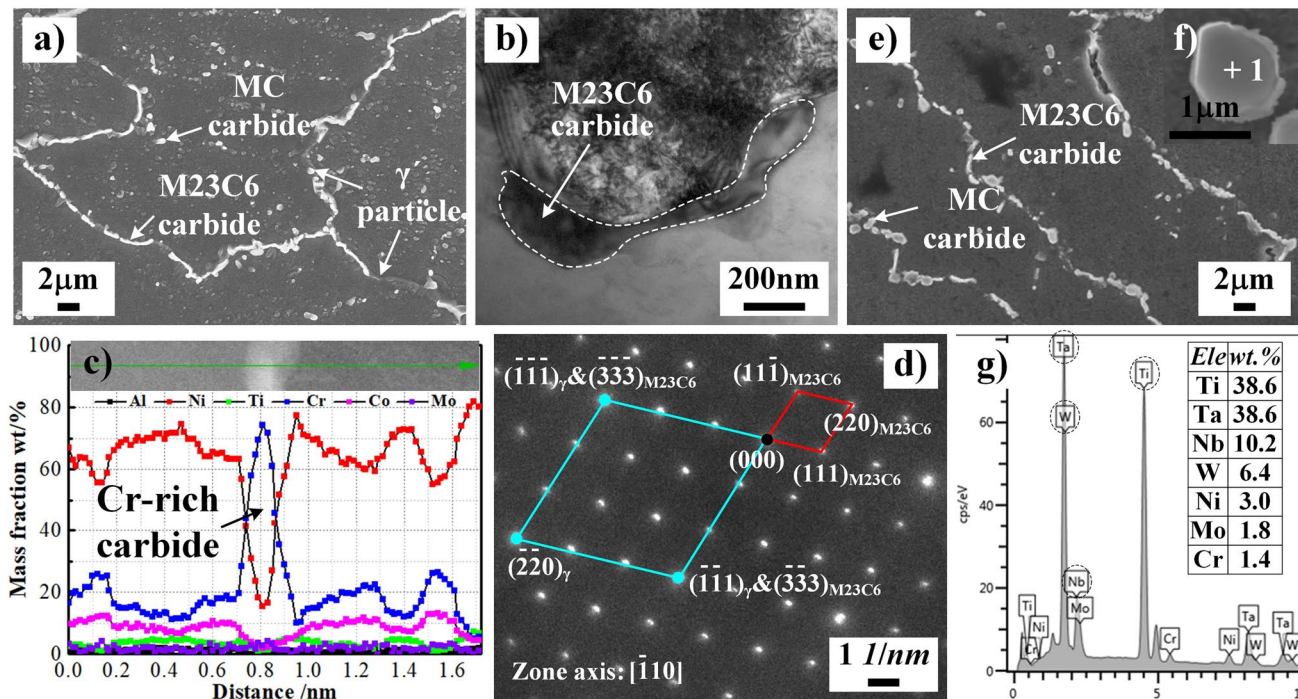
Fig. 5 Morphology and diffraction patterns of MC and M23C6 carbides in FZ of IN738LC joints subjected to different PWHTs: P-PWHT: **a** morphology, **b** TEM image, **c** elemental distribution, and **d** diffraction patterns of M23C6 carbide; F-PWHT: **e**, **f** morphology and **g** EDS mapping of MC carbide

the decomposition of MC carbide ($\gamma + MC \rightarrow \gamma' + M23C6$) [22] or precipitation from γ-Ni matrix ($\gamma \rightarrow M23C6 + \gamma'$) [23] were reported. Figure 5a and d illustrate that M23C6 carbides were mainly distributed along GBs, which proved that M23C6 carbides were precipitated by means of $\gamma \rightarrow M23C6 + \gamma'$ reaction. The block precipitates were distributed in IDR. EDS mapping displayed that Ta, Ti, and Nb were rich in the block precipitate, which was identified as (Ti, Ta, Nb)C (abbreviated as MC carbide). The partial

dissolution of MC carbides [24] in the process of solution treatment resulted in its morphology transformation from Chinese-script shape to block or spheroidal shape.

Figure 6 shows the distribution of M23C6 carbide in FZ of IN738LC joints subjected to PWHT. With the increased solution temperature, the thickness and length ratio (carbide length/GB length) of M23C6 carbides increased obviously. On the one hand, primary γ′ particles were dissolved completely at 1175 °C, resulting

Fig. 6 Thickness and length ratio of M23C6 carbides in FZ of IN738LC joints subjected to different PWHTs
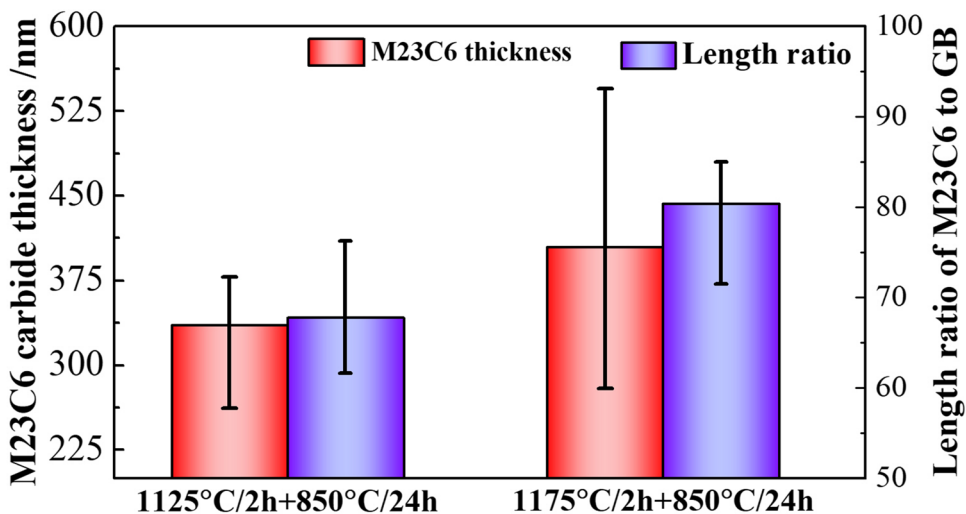
in enrichment of alloy elements (Al, Ti, and Cr) in IDR or GBs, as shown in Fig. 4. On the other hand, the previous work indicated that higher solution facilitated the dissolution of MC carbide, causing the obvious decrease of MC content from 1.22 (1125 °C/2 h) to 1.08% (1175 °C/2 h) [14]. The partial dissolution of MC carbides located in GBs released C atoms and provided a localized carbon reservoir. As a result, the enrichment of M23C6-forming elements aided in the precipitation of M23C6 carbides along GBs after F-PWHT.

3.1.2 *Heat-affected zone (HAZ) + BM*

The microstructures of HAZ and BM in IN738LC joints after different PWHTs are shown in Fig. 7. The joints after PWHT exhibited the similar microstructures, which were composed of γ′ particles, γ/γ′ eutectic, MC, and M23C6 carbides. Due to high energy density ($\geq 10^9$ W/m^2 [5]) and cooling rate (980 °C/s [25]) of EBW, a narrow HAZ about 0.2–0.5 mm was produced in as-weld joint. Therefore, we focused on the microstructural evolution of BM, and the statistical results in size and content of precipitates are shown in Table 4. After F-PWHT, the dual-sized γ′ particles were transformed into mono-sized γ′ particles in BM, which was consist with the microstructure in FZ. Moreover, γ/γ′ eutectic in BM was still visible and it further verified the above deduction about the formation of γ/γ′ eutectic in FZ. The size and amount of secondary γ′ particles in BM of IN738LC joint after F-PWHT were higher than that of P-PWHTed joint, which was related to the complete dissolution of primary γ′ particles during solution treatment. In addition, the increase in solution temperature

Table 4 The size and content of precipitates in BM of IN738LC joints subjected to different PWHTs

	Equivalent diameter/ nm		Volume fraction (%)		Area percent of MC carbide (%)
	Primary γ′	Secondary γ′	Primary γ′	Secondary γ′	
P-PWHT	670	101.3	6.94	43.99	1.1
F-PWHT	/	108.8	/	53.8	0.83

(1125 °C → 1175 °C) expedited the diffusion of MC-forming elements (D_{Ti}: 2.17×10^{-14} m^2/s → 4.92×10^{-14} m^2/s [26], D_{Ta}: 1.41×10^{-14} m^2/s → 2.70×10^{-14} m^2/s [27], and D_{Nb}: 2.90×10^{-14} m^2/s → $2.705.81 \times 10^{-14}$ m^2/s [28]), resulting in the increased amount of dissolved MC carbides (as seen in Table 4). However, the amount of M23C6 carbides in BM far lower than that of FZ. According to the classical dissolution model of precipitates [29], the dissolution rate of precipitates was inversely proportional to the size of precipitates. Compared with FZ, the larger MC carbide in BM delayed its dissolution, giving rise to less free C atoms at GBs. Consequently, the depletion of free C atoms in BM brought about a significant reduction of M23C6 carbides.

3.2 Evaluation of mechanical properties

3.2.1 Tensile properties (900 °C)

Figure 8 shows the tensile properties of IN738LC joints subjected to different PWHTs. It is notable that all the

Fig. 7 Microstructure of HAZ and BM in IN738LC joints after different PWHTs: P-PWHT: **a1** microstructure of HAZ; **b1** M23C6 carbides, **c1** microstructure, **d1** secondary γ′ particles, and **e1** primary γ′ particles in BM; F-PWHT: **a2** microstructure of HAZ; **b2** M23C6 carbides, **c2** microstructure, **d2** secondary γ′ particles, and **e2** γ/γ′ eutectic in BM
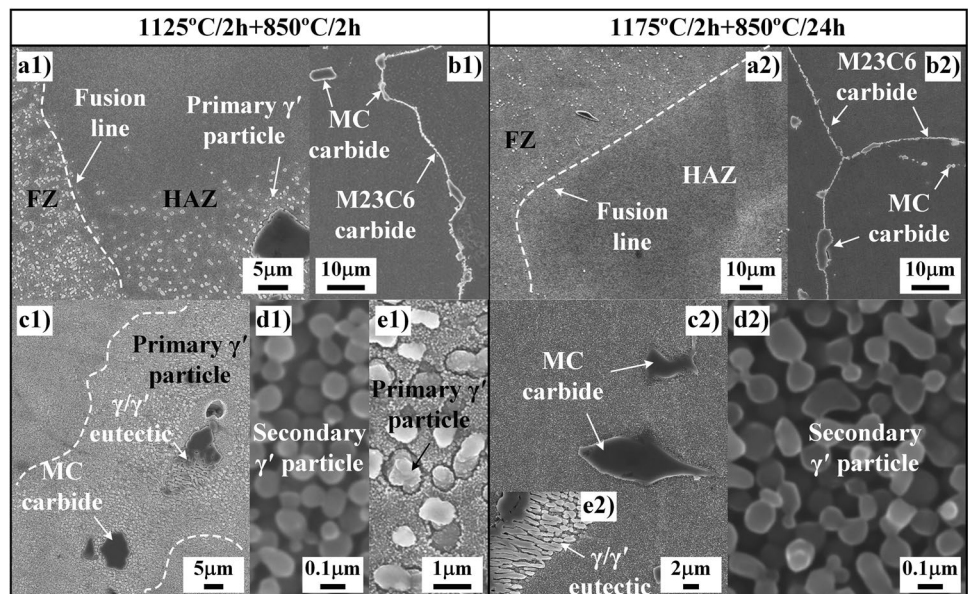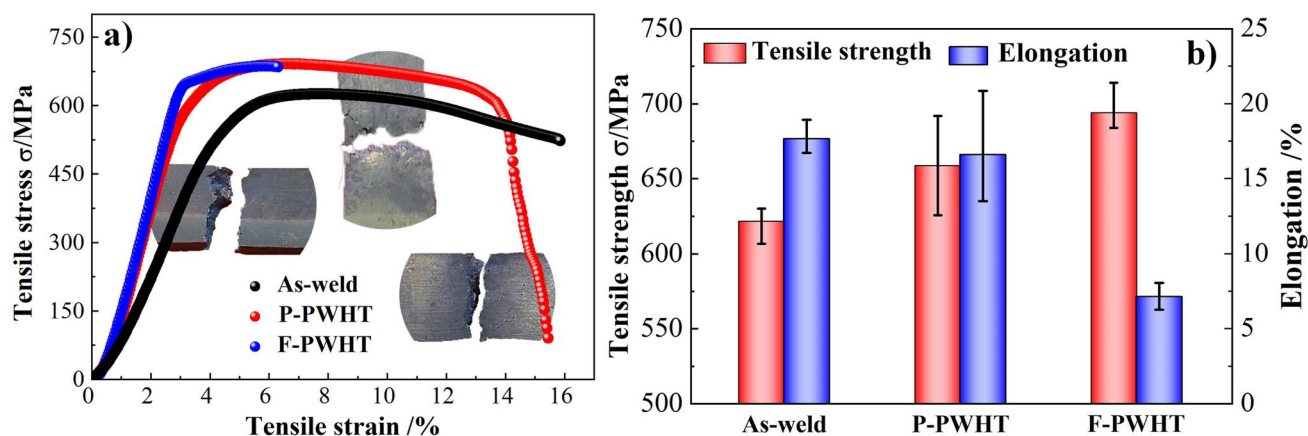
Fig. 8 Tensile strength and fracture location of IN738LC joint with different PWHTs at 900 °C: **a** stress–strain curve; **b** tensile strength and elongation

joints fractured in BM, confirming the weak zone of IN738LC joints. Compared with the as-weld joint, an increase in the tensile strength of IN738LC joints subjected to PWHT, which was due to the precipitation of γ′ particles. The joint subjected to F-PWHT showed a higher tensile strength but a significantly lower elongation than that of P-PWHTed joint, which was decided by the γ channel size and precipitate content in BM. On the one hand, higher amount of γ′ precipitates (54.8%) was present in BM after F-PWHT, showing a better intragranular strengthening effect [30]. On the other hand, the increase of solution temperature accelerated the dissolution of MC carbides. The full

dissolution of primary γ′ particles and the decreased content of MC carbides after F-PWHT resulted in the significant degradation of GB strength. Moreover, the deformation mechanism of nicker-based superalloy was Orowan bypassing mechanism at elevated temperature [31]. According to the expression (1) [32], the critical resolved shear stress increased when the channel width of γ-Ni matrix decreased. Owing to larger size (670 nm) of primary γ′ particles, the channel width was increased, causing a lower tensile strength of IN738LC joint subjected to P-PWHT. Based on the above-mentioned analysis, IN738LC joint with F-PWHT presented a higher tensile strength but lower elongation.

Fig. 9 Cross-section microstructure and fractured morphologies of IN738LC joints with different PWHT: P-PWHT: **a** cross-section microstructure; **b** cracked MC carbide; **c**, **d** fractured features; F-PWHT: **e** cross-section microstructure; **f**, **g** cracked MC carbide; **h**, **i**, **j** fractured features and microstructure
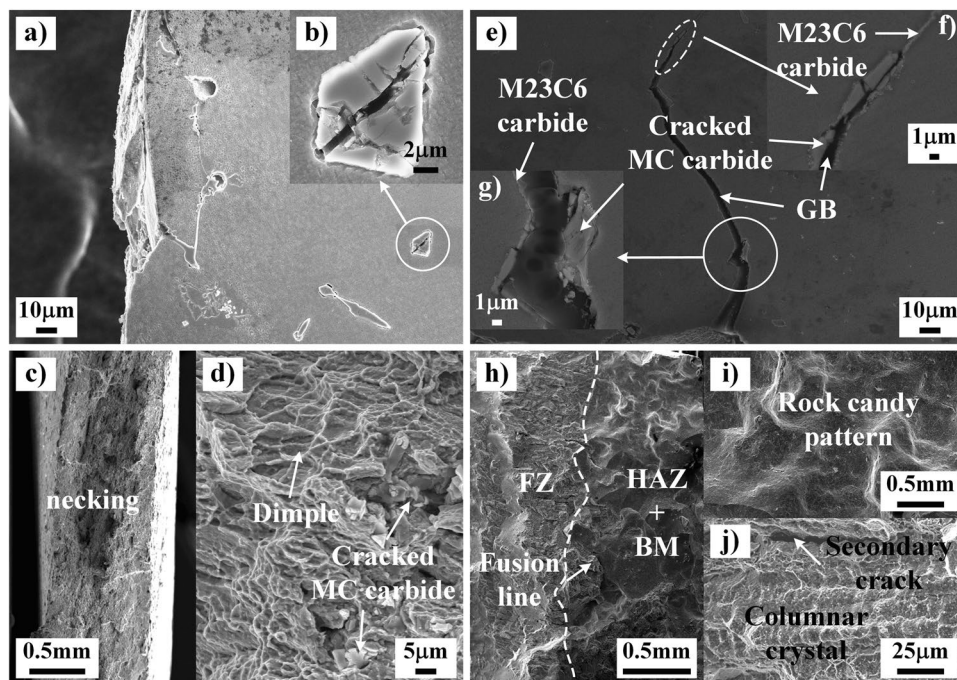
$$\tau_{OR} = \sqrt{\frac{2}{3}\frac{Gb}{l}} \qquad (1)$$

where G is the shear modulus, b denoted the Burger's vector, and l is the channel thickness along the ⟨110⟩ direction.

Figure 9 reveals the cross-section microstructure and fractured morphology of IN738LC joints subjected to P-PWHT and F-PWHT. Cracked MC carbides were visible in Fig. 9b. IN738LC joint also exhibited obvious necking feature and high density of dimples (Fig. 9d), indicating that IN738LC joint subjected to P-PWHT has excellent ductility (elongation: 16.6%). Thus, the joint after P-PWHT was broken in ductile fracture and transgranular fracture modes, while micro-cracks propagated along GBs in IN738LC joint subjected to F-PWHT, as shown in Fig. 9e. The fractured surface was relatively smooth and presented stone-like patterns. It is evident that the F-PWHTed joint obeyed the brittle fracture and intergranular fracture modes. The above transformation of fracture mode for IN738LC joint depended on the distribution of primary γ′ particles and MC carbides along GBs. Du et al. pointed out that the high stiffness of brittle MC carbides and γ/γ′ eutectic led to the accumulation of dislocation at the MC/matrix or eutectic/matrix phase interface [33]. Compared with the P-PWHTed joint, the primary γ′ particles in IDR were dissolved completely and more MC carbides in GBs were decomposed at full solution temperature (Fig. 7), resulting in an obvious reduction of GB strengthening effect. Therefore, micro-cracks were likely to nucleate at MC/matrix interface and propagate along GBs.

3.2.2 Stress-rupture test (900 °C/350 MPa)

Figure 10 demonstrates the stress-rupture results of IN738LC joints subjected to different PWHTs. The stress-rupture life of F-PWHTed joint decreased to 1.4 h, about 56% of P-PWHT joint (2.5 h). It has been reported in literatures [34, 35] that M23C6 carbides along GBs had a great influence on the stress-rupture and creep properties at elevated temperature for nickel-based superalloy. Continuous M23C6 carbides were easier to induce the nucleation of cracks by the M23C6/matrix interface debonding under tensile stress. The compared results of stress-rupture life between as-weld joints and PWHTed joints further proved that the formation of M23C6 carbides along GBs deteriorated the stress-rupture properties. Figure 5 indicated that more M23C6 carbides were formed along GBs in IN738LC joint after F-PWHT. Besides that, the presence of primary γ′ particles in P-PWHTed joint could impede GB sliding, improving the stress-rupture life of IN738LC joint. As a result, P-PWHT could elevate the mechanical properties of IN738LC joint.

The cross-section microstructure and fractured morphology of IN738LC joints after stress-rupture test were observed and the results are shown in Fig. 11. The failure regions of IN738LC joints subjected to PWHT were located in FZ/HAZ (seen in Fig. 11a and e). In addition, high-power SEM images (Fig. 11b and f) displayed that the micro-cracks propagated along GBs and the M23C6/matrix interface decohesion was clearly visible. Compared with BM, FZ produced high content of M23C6 carbides due to sufficient M23C6-forming elements (C, Cr, Mo) in IDR or GBs. Resultantly, FZ was easier to be a weakened area of IN738LC joint. Two typical features were present in the fractured surface. The typical columnar dendrites in FZ proved the intergranular fracture mode, which was in accord with the aforementioned analysis that micro-cracks propagated along GBs. However, the fractured features were different in HAZ and BM, as seen in Fig. 11c and g. Region 2 was uneven and composed of distinct tearing ridges, illustrating that region 2 was corresponding to transgranular fracture
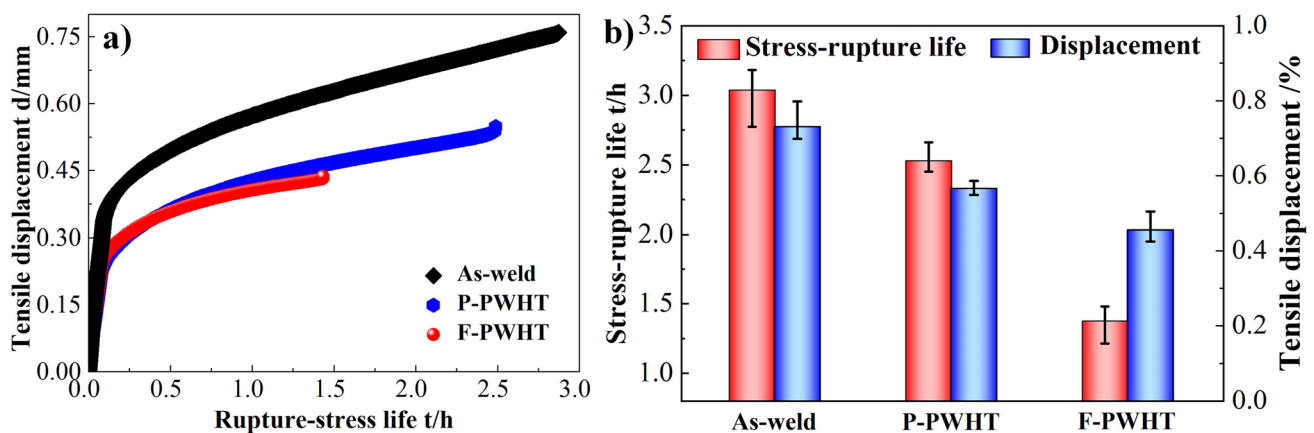

Fig. 10 Stress-rupture curves and life of IN738LC joints after different PWHTs at 900 °C/350 MPa: **a** stress-rupture curves; **b** stress-rupture life

Fig. 11 Cross-section microstructure and fractured morphology of IN738LC joints with different PWHTs: P-PWHT: **a**, **b** cross-section microstructure; **c**, **d** fractured morphology; F-PWHT: **e**, **f** cross-section microstructure; **g**, **h** fractured morphology
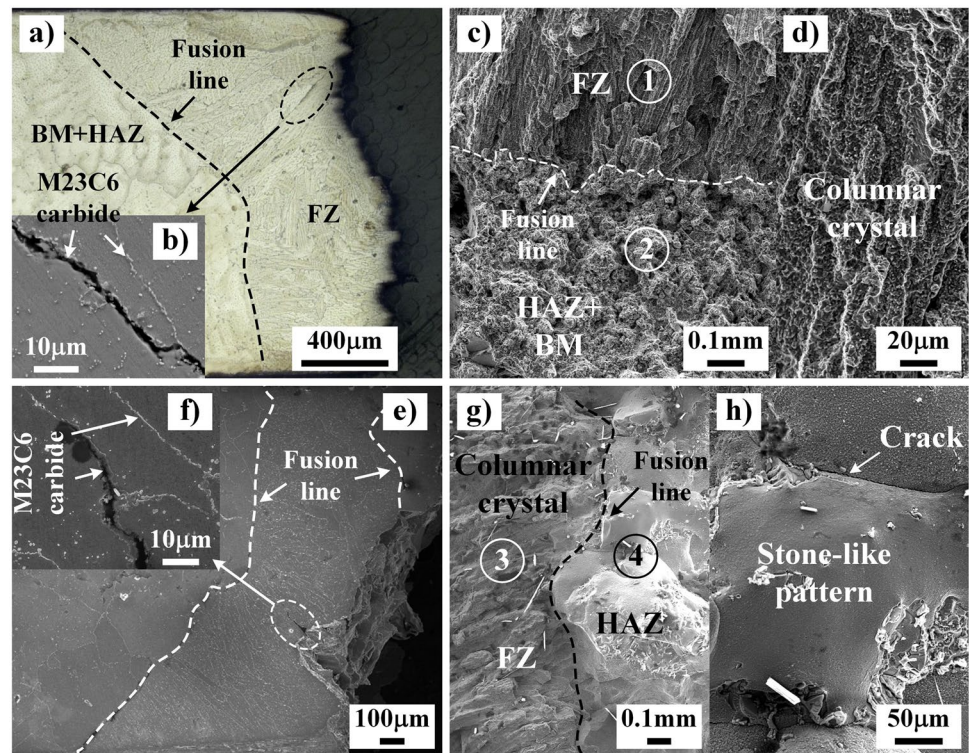
mode, while region 4 consisted of stone-like patterns, indicating that region 4 obeyed intergranular fracture mode. As a result, it further affirmed that P-PWHT was conducive to improving the mechanical properties of IN738LC joints.

4 Summary and conclusions

The effect of different PWHTs on the microstructure and mechanical properties of IN738LC EBWed joints was investigated. The conclusions can be drawn as follows:

(1) The two PWHT schedules produced the similar precipitates in IN738LC joints, consisting of γ′ particles, blocky MC carbides, and continuous M23C6 carbides. M23C6 carbides were mainly distributed along GBs.
(2) The primary γ′ particles were not dissolved completely in FZ and BM after P-PWHT, showing bimodal-sized γ′ particles. F-PWHT improved the complete dissolution of primary γ′ particles, reprecipitation, and growth of secondary γ′ particles. Therefore, the size and content of γ′ particles in FZ and BM after F-PWHT increased apparently. Higher solution temperature stimulated the dissolution of MC carbides by expediting the diffusion of MC-forming elements in FZ and BM, bringing about more M23C6 carbides in FZ and BM.
(3) The notable differences in the tensile strength, elongation, and rupture-stress life of IN738LC joints sub-jected to different PWHTs were observed. P-PWHT improved the tensile elongation (16.6%) but decreased the tensile strength of IN738LC joint as compared to that treated by F-PWHT. An obvious loss (45.5%) in rupture-stress life after F-PWHT was obvious due to the dissolution of primary γ′ particles and formation of more continuous M23C6 carbides in FZ.

Declarations

Conflict of interest The authors declare no competing interests.

References

1. Egbewande AT, Zhang HR, Sidhu RK, Ojo OA (2009) Improvement in laser weldability of INCONEL 738 superalloy through microstructural modification. Metall Mater Trans A 40:2694–2704

2. Mahmoudi H, Hadavi SMM, Palizdar Y (2021) Characterization, growth kinetics and formation mechanism of aluminide coating by plasma paste aluminizing on IN738. Vacuum 184:109968

3. Wang H, Zhang X, Wang GB, Shen J, Zhang GQ, Li YP, Yan M (2019) Selective laser melting of the hard-to-weld IN738LC superalloy: efforts to mitigate defects and the resultant microstructural and mechanical properties. J Alloys Compd 807:151662

4. Kong WW, Yuan C, Zhang BN (2020) Investigations on cyclic deformation behaviors and corresponding failure modes of a Ni-based superalloy. Mater Sci Eng A 791:139775

5. Węglowski MS, Błacha S, Phillips A (2016) Electron beam welding–techniques and trends–review. Vacuum 130:72–92

6. Wang W, Jiang L, Li C, Leng B, Ye X, Liu R, Chen S, Yu K, Li Z, Zhou X (2019) Effects of post-weld heat treatment on microstructure and mechanical properties of Hastelloy N superalloy welds. Mater Today Commun 19:230–237

7. Xu Y, Li W, Yang X, Gu Y (2020) Evolution of grain structure, γ' precipitate and hardness in friction welding and post weld heat treatment of a new Ni-Fe based superalloy [J]. Mater Sci Eng A 788:139596

8. Liburdi J, Lowden P, Nagy D, De Priamus TR, Shaw S (2009) Practical experience with the development of superalloy rejuvenation. ASME Turbo Expo 4:819–827

9. Chang JC, Choi C, Kim JC, Yun YH (2003) Development of microstructure and mechanical properties of a Ni-base single-crystal superalloy by hot-isostatic pressing. J of Materi Eng and Perform 12:420–425

10. Balikci E, Raman A, Mirshams RA (1997) Influence of various heat treatments on the microstructure of polycrystalline IN738LC. Metall Mater Trans A 28(10):1993–2003

11. Monti C, Giorgetti A, Tognarelli L, Mastromatteo F (2017) On the effects of the rejuvenation treatment on mechanical and microstructural properties of IN-738 superalloy. J Mater Eng Perform 26(5):2244–2256

12. Wangyao P, Homkrajai W, Asavavisithchai S (2009) Effect of post weld heat treatments on TIG-welded microstructures of superalloy IN-738. Chiang Mai J Sci 36:320–330

13. Jurado M, Altamirano G, Acevedo JL, Aguirre A (2019) Microstructural characterization of the laser welding in a nickel based superalloy. MRS Adv 4:3463–3473

14. Wang H, Han K, Zhang B (2021) Effect of post-weld solution treatment on microstructure and mechanical properties of electron beam welded IN738LC joint. J Mater Res Technol 15:3047–3059

15. Ou M, Ma Y, Hou K, Wang M, Ma G, Liu K (2021) Effect of grain boundary precipitates on the stress rupture properties of K4750 alloy after long-term aging at 750°C for 8000 h. J Mater Sci Technol 92:11–20

16. Taheri M, Halvaee A, Kashani-Bozorg SF (2021) Effect of pre- and post-weld heat treatment on microstructure and mechanical properties of GTD-111 superalloy welds. Met Mater Int 27(5):1173–1192

17. Han K, Wang H, Peng F, Zhang B, Shen L (2018) Investigation of microstructure and mechanical performance in IN738LC joint by vacuum electron beam welding. Vacuum 162:214–227

18. He L, Zheng Q, Sun X, Guan HR, Hu ZQ, Tieu K, Lu C, Zhu H (2005) Effect of heat treatment on microstructures and tensile properties of Ni-base superalloy M963. Mater Sci Eng A 398:128–136

19. Li Q, Xie J, Yu JJ, Shu D, Hou G, Sun X, Zhou Y (2021) Solidification behavior and segregation characteristics of high W-content cast Ni-based superalloy K416B. J Alloy Compd 854:156027

20. Zhang Z, Zhao Y, Shan J, Wu AS, Sato Y, Tokita S, Kadoi K, Inoue H, Gu H, Tang X (2021) Evolution behavior of liquid film in the heat-affected zone of laser cladding non-weldable nickel-based superalloy. J Alloy Compd 863:158463

21. Dong C, Liu Z, Chen Z, Bao H, Wang X, Liu Z (2020) Carbide dissolution and grain growth behavior of a nickel-based alloy without γ' phase during solid solution. J Alloy Compd 825:154106

22. Sun W, Qin X, Guo J, Lou L, Zhou L (2015) Thermal stability of primary MC carbide and its influence on the performance of cast Ni-base superalloys. Mater Design 69:81–88

23. Jiang L, Hu R, Kou H, Li J, Bai G, Fu H (2012) The effect of M23C6 carbides on the formation of grain boundary serrations in a wrought Ni-based superalloy. Mater Sci Eng A 536:37–44

24. Cowen CJ, Danielson PE, Jablonski PD (2011) The microstructural evolution of Inconel alloy 740 during solution treatment, aging, and exposure at 760 °C. J of Materi Eng and Perform 20:1078–1083

25. Han K, Wang H, Peng F, Zhang B, Guo L (2020) Effect of thermal compensation treatment on the microstructure and mechanical properties of IN738LC joint by electron beam welding. J Manuf Process 58:536–550

26. Masoumi F, Jahazi M, Shahriari D, Cormier J (2016) Coarsening and dissolution of γ' precipitates during solution treatment of AD730™ Ni-based superalloy: mechanisms and kinetics models. J Alloy Compd 658:981–895

27. Karunaratne MSA, Carter P, Reed RC (2000) Interdiffusion in the face-centred cubic phase of the Ni–Re, Ni–Ta and Ni–W systems between 900 and 1300ºC. Mater Sci Eng A 281:229–233

28. Karunaratne M, Reed RC (2005) Interdifusion of niobium and molybdenum in nickel between 900–1300ºC. Defect Diffus Forum 237:420–425

29. Semiatin SL, Levkulich NC, Saurber AE, Mahaffey DW, Payton EJ, Senkov ON (2017) The kinetics of precipitate dissolution in a nickel-base superalloy. Metall Mater Trans A 48:5567–5578

30. Reed RC (2006) The superalloys: fundamentals and applications. Cambridge: Cambridge University Press, UK, 85.

31. Cui L, Su H, Yu J, Liu J, Jin T, Sun X (2017) Temperature dependence of tensile properties and deformation behaviors of nickel-base superalloy M951G. Mater Sci Eng A 696:323–330

32. Pollock TM, Argon AS (1992) Creep resistance of CMSX-3 nickel base superalloy single crystals. Acta Metall Mater 40:1–30

33. Du B, Hu Z, Sheng L, Cui C, Yang J, Zheng Y, Sun X (2018) Tensile, creep behavior and microstructure evolution of an as-cast Ni-based K417G polycrystalline superalloy. J Mater Sci Technol 34(10):1805–1816

34. He LZ, Zheng Q, Sun XF, Guan HR, Hu ZQ, Tieu AK, Lu C, Zhu HT (2005) Effect of carbides on the creep properties of a Ni-base superalloy M963. Mater Sci Eng A 397:297–304

35. Guo Y, Wang B, Hou S (2013) Aging precipitation behavior and mechanical properties of Inconel 617 superalloy. Acta Metall Sin-Engl 26:307–312